

# First-Principles Study of Novel Two-Dimensional $(C_4H_9NH_3)_2PbX_4$ Perovskites for Solar Cell Absorbers

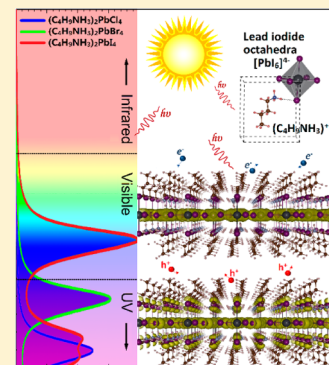
Da Wang,<sup>†,ID</sup> Bo Wen,<sup>†,‡</sup> Ya-Nan Zhu,<sup>†</sup> Chuan-Jia Tong,<sup>†</sup> Zhen-Kun Tang,<sup>†</sup> and Li-Min Liu<sup>\*,†,ID</sup>

<sup>†</sup>Beijing Computational Science Research Center, Beijing 100193, People's Republic of China

<sup>‡</sup>International Center for Quantum Materials (ICQM) and School of Physics, Peking University, Beijing, 100871, People's Republic of China

## Supporting Information

**ABSTRACT:** Low-dimensional perovskites ( $A_2BX_4$ ), in which the A cations are replaced by different organic cations, may be used for photovoltaic applications. In this contribution, we systematically study the two-dimensional (2D)  $(C_4H_9NH_3)_2PbX_4$  ( $X=Cl, Br$  and  $I$ ) hybrid perovskites by density functional theory (DFT). A clear structures–properties relationship, with the photophysical characteristics directly related to the dimensionality and material compositions, was established. The strong  $s-p$  antibonding couplings in both bulk and monolayer  $(C_4H_9NH_3)_2PbI_4$  lead to low effective masses for both holes ( $m_h^*$ ) and electrons ( $m_e^*$ ). However,  $m_h^*$  increases in proportion to the decreasing inorganic layer thickness, which eventually leads to a slightly shifted band edge emission found in 2D perovskites. Notably, the 2D  $(C_4H_9NH_3)_2PbX_4$  perovskites exhibit strong optical transitions in the visible light spectrum, and the optical absorption tunings can be achieved by varying the compositions and the layer thicknesses. Such work paves an important way to uncover the structures–properties relationship in 2D perovskites.



In the present decade, hybrid halide perovskites have been the most striking development in the area of photovoltaics for the best choice in covering the needs of low-cost manufacture and high efficiency.<sup>1–3</sup> Since the first report of a stable solar cell based on  $CH_3NH_3PbI_3$  (MAPbI<sub>3</sub>) perovskite in 2012, their photovoltaic performance races have been remarkable ever since, and an efficiency of 20.1% has been confirmed by a national renewable energy laboratory,<sup>4</sup> exceeding all other solar cells manufactured by solution processing methods.<sup>5</sup> To further extend the adsorption range (mainly toward the near-IR region) and improve the charge transport properties as well as the stability, a great effort is being devoted to investigate other perovskites, differing from MAPbI<sub>3</sub> for the choice of halogenide, metal cation, and ammonium ion.<sup>6–10</sup> This effort is also strongly supported by high level theoretical modeling,<sup>11–15</sup> which has proved very useful to prescreen the various materials and to help the interpretation of the experimental data.

Early pioneering research<sup>16</sup> in hybrid halide perovskites fields have clearly demonstrated that the  $APbX_3$  perovskite is a potential candidate for a two-dimensional (2D) optical system with tunable property, allowing for the development of new types of perovskites for solar cell beyond MAPbX<sub>3</sub>. As the perovskite structure is cut into slices, the size restrictions, as outlined by the Goldschmidt tolerance factor for the 3D structures, are gradually lifted. For example, in two-dimensional (2D) layered derivatives of the perovskite structure, there are no known restrictions for the interlayer "A" cation length. This structural flexibility and tunability of the dimensionality provide a rich and fertile "playground" for the preparation of interesting

crystal structures with varying physical properties. For this reason, significant efforts are presently being made to synthesize and characterize these novel materials.<sup>17–23</sup>

The atomically thin 2D  $(C_4H_9NH_3)_2PbX_4$  ( $X=Cl, Br$  and  $I$ ) hybrid perovskites could be synthesized in solution and were thus relatively simple to produce compared with many other atomically thin 2D materials, which are made by mechanical exfoliation or by chemical vapor/atomic layer deposition.<sup>22,24</sup> The atomically thin 2D regime of the  $(C_4H_9NH_3)_2PbX_4$  hybrid perovskites provides unique opportunities for tuning the electronic structure, for example, by substrate interactions, mechanical strain, quantum confinement (layer thickness), stacking of different atomically thin 2D crystals to create van der Waals heterostructures,<sup>25</sup> or by varying the size of the alkyl chains.<sup>26</sup> The bottom-up approach recently demonstrated for a layer-by-layer synthesis of the atomically thin 2D perovskites has also opened up a new frontier to synthesize and tailor the properties of these compounds.<sup>22,27</sup> Although 2D  $(C_4H_9NH_3)_2PbX_4$  perovskites with suitable band gaps could be very interesting for applications in mesoscopic solar cells, they have not been systematically studied for photovoltaic applications so far, and the fundamental mechanisms concerning whether these 2D perovskites can perform well as solar cell absorbers are still unclear. Thus, there are great interests to evaluate how the behavior of the structure and the intercalates, for instance, the layer thickness, the size of the

Received: January 1, 2017

Accepted: February 3, 2017

Published: February 3, 2017

alkyl chain, the charge, or the ability to form hydrogen bonds influences the electronic properties of 2D perovskite.

In this paper, we focus on a new type of 2D hybrid perovskite,  $(C_4H_9NH_3)_2PbX_4$  ( $X = Cl, Br$  and  $I$ ) at the level of density functional theory (DFT). A relatively lower surface energy was found in 2D  $(C_4H_9NH_3)_2PbI_4$  perovskite compared to conventional  $APbX_3$  perovskites, confirming the convenient preparation of atomically thin 2D hybrid perovskites experimentally. Additionally, a clear relationship between the photophysical properties and the dimensionality and material composition was established. Small effective masses for both hole ( $m_h^*$ ) and electron ( $m_e^*$ ) were found in both bulk and monolayer  $(C_4H_9NH_3)_2PbI_4$ , contributing by the strong  $s-p$  antibonding couplings that occurred at the conduction band minimum (CBM) and valence band maximum (VBM). However,  $m_h^*$  increases in proportion to the decreasing inorganic layer thickness, which eventually leads to a easier bondage of the excitons found in 2D perovskites. Notably, the calculated optical absorption coefficients suggest that the 2D  $(C_4H_9NH_3)_2PbX_4$  perovskites are effective solar energy absorbers in visible light spectra. More importantly, ultrahigh optical absorptions enable the use of the 2D  $(C_4H_9NH_3)_2PbX_4$  absorber where the photogenerated carrier does not have to travel long distances before it is collected, and eventually leads to a lower rate of the nonradiative recombination process.

First-principles calculations were performed using the Vienna Ab initio Simulation Package (VASP),<sup>28,29</sup> a periodic density functional theory (DFT) code utilizing a plane-wave basis set, with interactions between the core and valence electrons described using the projector augmented wave (PAW) method.<sup>30–32</sup> Owing to the large spin-orbit coupling (SOC) constant of the lead atom, the spin-orbit coupling effect on the band structures of  $(C_4H_9NH_3)_2PbX_4$  are considered to be significant. The DFT-D3 approach was used to evaluate the effect of the van der Waals (vdW) interaction.<sup>33</sup> To investigate the origin of the band gaps and the nature of chemical bondings more realistically, many functionals, including the Perdew, Burke, and Ernzerhof (PBE) functional<sup>34</sup> and the Heyd Scuseria Ernzerhot (HSE06) hybrid functional,<sup>35</sup> are employed in our study. The HSE06 functional, which incorporates  $\alpha = 35\%$  of Hartree–Fock exact exchange contribution and  $1 - \alpha = 65\%$  of PBE contribution reproduced the experimental bandgap of  $(C_4H_9NH_3)_2PbX_4$  and interpreted well the lower conduction bands originated from Pb  $6p$  orbitals. (as shown in Table S1 and Figure 2a). Thus, the HSE06 with  $\alpha = 35\%$  is used in the following discussion. A large plane wave cutoff of 450 eV and  $3 \times 3 \times 3$  and  $3 \times 3 \times 1$  with  $\Gamma$  centered k-point sampling are used for the bulk and 2D cells of  $(C_4H_9NH_3)_2PbI_4$ . For structural relaxation, the ionic force is converged to 0.01 eV  $\text{\AA}^{-1}$ . Each structure is first relaxed at a single k-point using the HSE06 ( $\alpha = 35\%$ ) before the band gap is obtained using HSE06+SOC.

For the optical property calculation, the imaginary parts of the dielectric functions because of the direct interband transitions are defined as follows.<sup>36</sup>

$$\epsilon_2(\hbar\omega) = \frac{2e^2\pi}{\Omega\epsilon_0} \sum_{k,v,c} |\langle \psi_k^c | u_r | \psi_k^v \rangle|^2 \delta(E_k^c - E_k^v - E) \quad (1)$$

where  $c, v, u, \omega$  and  $\Omega$  are conduction bands, valence bands, the vector defining the polarization of the incident electric field, photon frequencies, and the unit-cell volume, respectively. The

exciton binding energy ( $E_b$ ) was obtained following the methodology of Jong et al.<sup>37</sup>

$$E_b \approx 13.56 \cdot \frac{m_r^*}{m_e} \cdot \frac{1}{\epsilon^2} (\text{eV}) \quad (2)$$

where  $m_r^*/m_e$  and  $\epsilon$  indicate the effective mass of hole/electron and the static dielectric constant of materials.

Figure 1c,d shows the top and side views of the cubic structure, respectively; the primitive cell of 2D

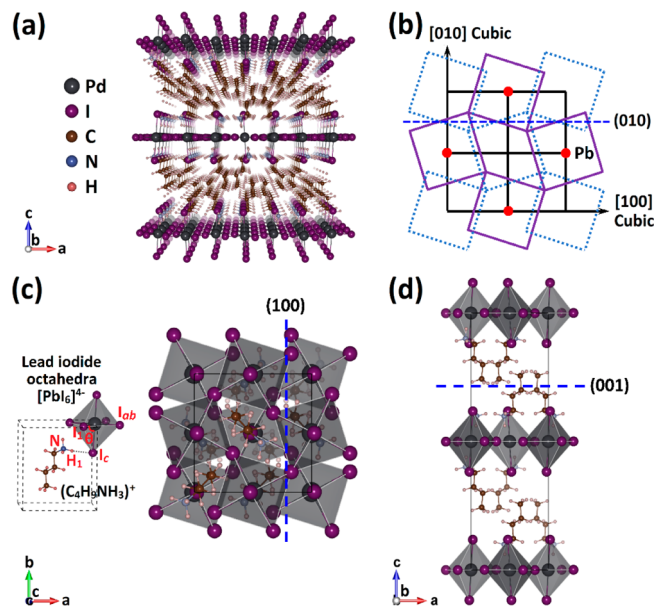


**Figure 1.** (a,b) Crystal structure for 2D  $(C_4H_9NH_3)_2PbX_4$  ( $X = Cl, Br, I$ ) perovskites. (c,d) Optimized structure of  $(C_4H_9NH_3)_2PbX_4$  as viewed along the [001] and [010] directions, respectively. Blue dashed lines indicate the representative (100) and (001) planes.

$[(C_4H_9NH_3)_2PbX_4]_4$  crystals contain four formula units. Table S1 summarizes the calculated and literature band gaps, lattice parameters and volumes. Compared with the PBE, PBE +soc and HSE functionals, the HSE+soc provides a better result, as it usually does for semiconductors.<sup>38</sup> More importantly, as  $\alpha = 35\%$ , the HSE+SOC method reproduced the experimental band gaps and gave the lattice constants and volume in 5% errors from the experimental values at room-temperature. For example, it predicts a direct bandgap of 3.602 eV, which agrees reasonably well with the experimental bandgap, 3.735 eV<sup>40</sup> (direct), measured from the  $(C_4H_9NH_3)_2PbCl_4$ . Thus, we used the  $HSE^{\alpha=0.35}+SOC$  method to evaluate the electronic properties of 2D  $(C_4H_9NH_3)_2PbX_4$  perovskites. This is also consistent with the previous studies suggesting that in a conventional three-dimensional (3D)  $MAPbI_3$  perovskite, when the SOC is considered, which is necessary for correctly interpreting the lower conduction band derived from Pb  $6p$  states,<sup>39</sup> the Heyd–Scuseria–Ernzerhof (HSE) hybrid functional with a Hartree–Fock portion ( $\alpha$ ) as large as 43% needs to be used to correctly predict the bandgap.<sup>41,42</sup>

We further calculate the electronic properties of  $(C_4H_9NH_3)_2PbX_4$ . Figure 2a and 2b show the PDOS and bonding diagram of the 2D  $(C_4H_9NH_3)_2PbX_4$  systems. The valence bands (VB) consist of Pb (6s)-I (5p) antibonding states, nonbonding I (5p) states and Pb (6p)-I (5p) states with

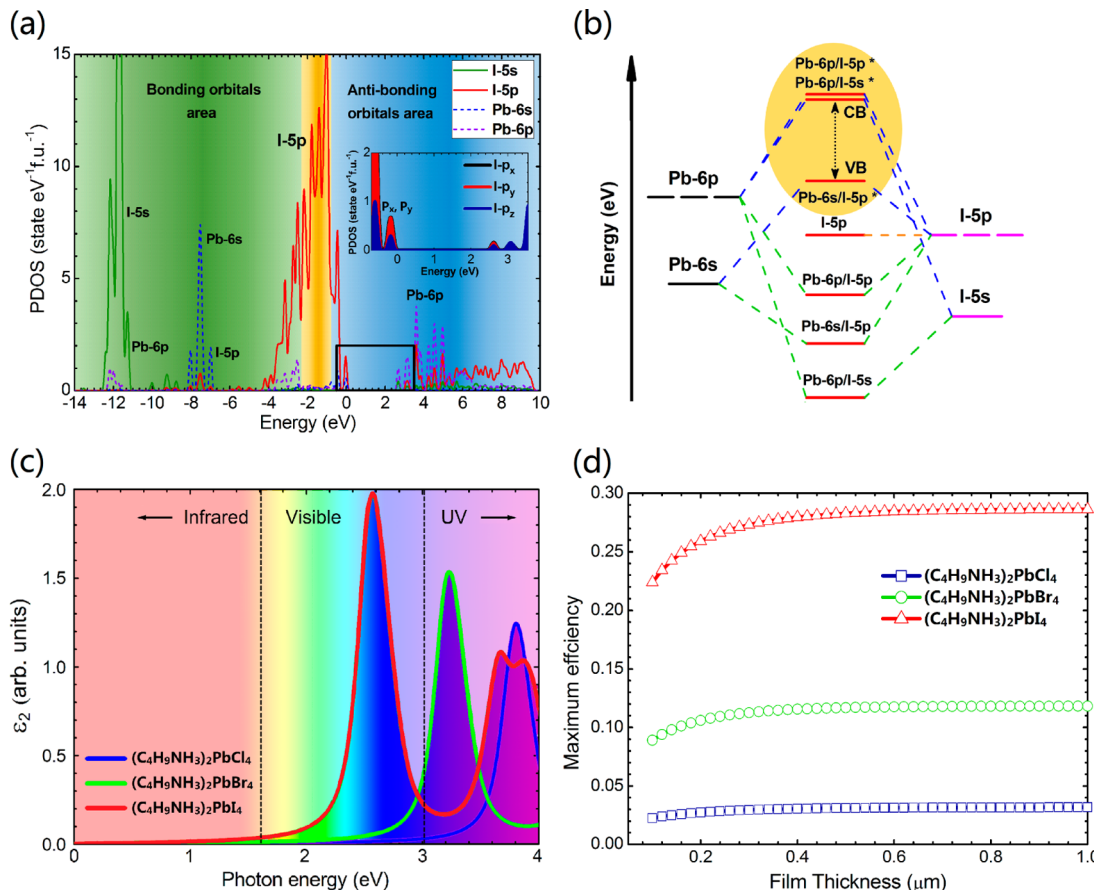


**Figure 2.** (a) The partial density of states (PDOS) of 2D  $(C_4H_9NH_3)_2PbI_4$ . (b) Schematic of the band alignment between Pb-6s/6p and I-5s/5p. (c) Imaginary part of the dielectric function,  $\epsilon_2$ , as a function of photon energy  $\hbar\omega$  for  $(C_4H_9NH_3)_2PbI_4$ . (d) Calculated maximum efficiencies of  $(C_4H_9NH_3)_2PbX_4$  ( $X = Cl, Br, I$ ) as a function of film thickness.

their band widths calculated to be 1.031, 1.473, and 2.016 eV, respectively. Below the valence bands, other Pb (6s) states, which are slightly hybridized with I (5p) orbital, are found to localize within -6.81 and -8.23 eV. The Pb (6p)-I (5s) antibonding states formed in the deeper position between -6.807 and -8.279 eV, and have almost no contribution to the valence bands. Additionally, The lowest unoccupied band consists of Pb (6p)-I (5s) s-antibonding and Pb (6p)-I (5p) p-antibonding states.

To directly estimate the light trapping capability of 2D halide perovskites, the photoabsorption coefficients of  $(C_4H_9NH_3)_2PbX_4$  ( $X = Cl, Br, I$ ) are evaluated, which can be obtained from Equation 1 using the real and imaginary parts of frequency dependent dielectric constants, calculated by HSE +soc. As shown in Figure 2c, the absorptions of  $(C_4H_9NH_3)_2PbI_4$ ,  $(C_4H_9NH_3)_2PbBr_4$ , and  $(C_4H_9NH_3)_2PbCl_4$  along the [100] and [010] directions exhibit a peak at 2.559, 3.225, and 3.799 eV, respectively, and there is no noticeable absorption below 2.0 eV. It is suggested that the large absorption features of 2D halide perovskites mainly come from two aspects: (i) The direct bandgaps, which can effectively excite electrons without the assistance of a phonon; e.g.,  $(C_4H_9NH_3)_2PbI_4$ ,  $(C_4H_9NH_3)_2PbBr_4$ , and  $(C_4H_9NH_3)_2PbCl_4$ , have direct bandgaps of 2.293, 2.987, and 3.602 eV, respectively. (ii) The achievement of  $p-p$  transitions. The Pb has a  $6s^2$  electron configuration, what we call a lone-pair s electron.<sup>43</sup> In 2D  $(C_4H_9NH_3)_2PbX_4$ , the s electrons would not be lost, so the deeper part of conduction band mainly originates

from the unoccupied Pb (p) states (Figure 1a). Also, the upper valence bands are mainly attributed by I (p) states mixed with a little contribution of Pb (s) orbitals. This makes the  $p-p$  transitions found in  $(C_4H_9NH_3)_2PbX_4$ . Because the p orbital has two more orbitals than s orbital and exhibits less dispersion, the direct bandgap  $p-p$  transitions are commonly considerably larger than  $s-p$  transitions, which are generally seen in the conventional solar energy absorbers such as GaAs, CdTe, CIGS, and  $Cu_2ZnSnSe_4$  (CZTSe), as indicated by Yin et al.<sup>11</sup> in previous work.

Notably, for  $(C_4H_9NH_3)_2PbI_4$  system, the mixed halide perovskites exhibit the extended absorption character over the whole visible light spectrum, which is an advantageous property for light harvesting because the visible light region takes up the main useable part of the whole solar spectrum.<sup>11,44</sup> For  $(C_4H_9NH_3)_2PbBr_4$  and  $(C_4H_9NH_3)_2PbCl_4$  systems, however, the absorption onset gradually shifts to the higher photon energy, i.e., to shorter wavelength light. These blue-shifts of the absorption onsets could be readily expected from the rise of band gaps in the mixed halide perovskites  $(C_4H_9NH_3)_2PbX_4$  with the increase of halogen element.

The absorption coefficients significantly affect the quantum-efficiencies of the solar energy absorbers, yet they are not included in Shockley–Queisser limits.<sup>45</sup> Actually, the theoretical-maximum-efficiencies depended on the absorber thickness. Considering the layer thickness and the absorption coefficients, the maximum efficiencies of 2D  $(C_4H_9NH_3)_2PbX_4$  as a function of layer thickness were calculated following the methodology of

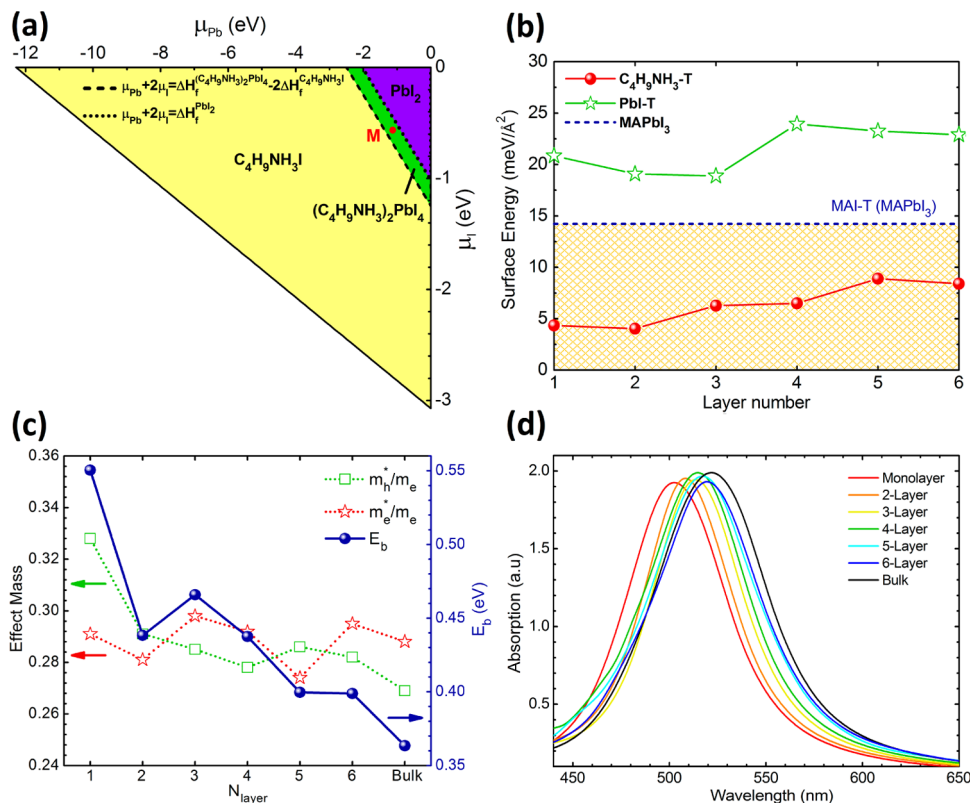


**Figure 3.** (a) Thermodynamically stable ranges of Pb and I chemical potential under the equilibrium growth conditions of  $(\text{C}_4\text{H}_9\text{NH}_3)_2\text{PbI}_4$ . (b) The calculated surface energies of  $\text{C}_4\text{H}_9\text{NH}_3\text{-T}$  and  $\text{PbI-T}$  as a function of layer number. Also, the surface energy of a conventional  $\text{MAPbX}_3$  perovskite with MAI-T termination is shown for comparison. (c) Calculated effective masses of electron ( $m_e^*/m_e$ ) and hole ( $m_h^*/m_e$ ), exciton binding energy ( $E_{\text{eb}}$ ) and (d) absorption coefficients of  $(\text{C}_4\text{H}_9\text{NH}_3)_2\text{PbI}_4$  with different layer numbers.

Yin et al.,<sup>11</sup> as shown in Figure 2d. The  $(\text{C}_4\text{H}_9\text{NH}_3)_2\text{PbI}_4$  halide perovskite exhibits much higher efficiencies than  $(\text{C}_4\text{H}_9\text{NH}_3)_2\text{PbBr}_4$  and  $(\text{C}_4\text{H}_9\text{NH}_3)_2\text{PbCl}_4$  in the whole range. More importantly,  $(\text{C}_4\text{H}_9\text{NH}_3)_2\text{PbI}_4$  perovskite can achieve a large efficiency even at a very thin layer, e.g., at 0.3  $\mu\text{m}$  thickness (similar to the size of  $\text{CH}_3\text{NH}_3\text{PbI}_{3-x}\text{Cl}_x$  based perovskites with the efficiency of 15.4%),<sup>46</sup> the maximum efficiency of  $(\text{C}_4\text{H}_9\text{NH}_3)_2\text{PbI}_4$  perovskite could be achieved to 27%, while they are only 11% and 3% for  $(\text{C}_4\text{H}_9\text{NH}_3)_2\text{PbBr}_4$  and  $(\text{C}_4\text{H}_9\text{NH}_3)_2\text{PbCl}_4$  solar cells, respectively. The results are also consistent with the finding in several greatest common thin-film solar energy absorbers (CZTSS, CIGS, CdTe and GaAs) indicated that the thickness of solar cells should reach about 2  $\mu\text{m}$  to achieve a high efficiency.<sup>47</sup>

We next calculate the surface energies of different  $(\text{C}_4\text{H}_9\text{NH}_3)_2\text{PbX}_4$  terminations to examine the thermodynamical stability of this new type of 2D perovskite under the experimental conditions. Due to the layered structure of  $(\text{C}_4\text{H}_9\text{NH}_3)_2\text{PbX}_4$ , DFT calculations are conducted on a simple (001) surface. Here we take  $(\text{C}_4\text{H}_9\text{NH}_3)_2\text{PbI}_4$  as an example, as illustrated in Figure 1b, and the tetragonal (001) planes are constructed with the neutral  $[(\text{C}_4\text{H}_9\text{NH}_3)_2\text{I}_2]^0/[\text{PbI}_2]^0$  layers, that is, they are nonpolar surfaces. However, whether the molecule or I was terminated at the surface region is still unclear.<sup>48</sup> Under the growth conditions of  $(\text{C}_4\text{H}_9\text{NH}_3)_2\text{PbI}_4$  in the thermodynamic equilibrium, the existence of  $(\text{C}_4\text{H}_9\text{NH}_3)_2\text{PbI}_4$  should satisfy

$$2\mu_{\text{C}_4\text{H}_9\text{NH}_3} + \mu_{\text{Pb}} + 4\mu_{\text{I}} = \Delta H_f^{(\text{C}_4\text{H}_9\text{NH}_3)_2\text{PbI}_4} \quad (3)$$

where  $\mu_i$  is the chemical potentials of different elements, and  $i$  refers to their corresponding stable phase.  $\Delta H_f^{(\text{C}_4\text{H}_9\text{NH}_3)_2\text{PbI}_4}$  is the formation enthalpy of  $(\text{C}_4\text{H}_9\text{NH}_3)_2\text{PbI}_4$ . The following conditions should be requested to avoid forming the undesired secondary phase, such as  $\text{PbI}_2$  and  $\text{C}_4\text{H}_9\text{NH}_3\text{I}$ :

$$2\mu_{\text{C}_4\text{H}_9\text{NH}_3} + \mu_{\text{I}} < \Delta H_f^{(\text{C}_4\text{H}_9\text{NH}_3)_2\text{PbI}_4} \quad (4)$$

$$\mu_{\text{Pb}} + 2\mu_{\text{I}} < \Delta H_f^{\text{PbI}_2} \quad (5)$$

To satisfy eqs 3–5, the chemical potentials of Pb and I are limited in a narrow and long region as shown by the green color in Figure 3a. This range indicates the equilibrium growth conditions for synthesizing the  $(\text{C}_4\text{H}_9\text{NH}_3)_2\text{PbI}_4$  phase. The purple region on the upper right in Figure 3a indicates the  $\text{PbI}_2$ -rich environment; on the contrary, the yellow region on the lower left corresponds to a  $\text{C}_4\text{H}_9\text{NH}_3\text{I}$ -rich environment. The relation of chemical potentials indicate that the synthetic environment should be rigorously constrained in the preparation of  $(\text{C}_4\text{H}_9\text{NH}_3)_2\text{PbI}_4$  perovskites.

It is well-known that the morphology and architecture of the light harvester significantly affect the performance of the solar cells. The balance between epitaxial strains and surface energies, and between kinetics and energetics, usually dominates the facet growth in absorber films and the surface morphologies. Here, the slab models in our study contain equivalent top and bottom surfaces with different stoichiometry from the bulk. To examine the relative stabilities of both terminations, the surface energies were calculated based on the chemical potentials of constituent elements determined above:

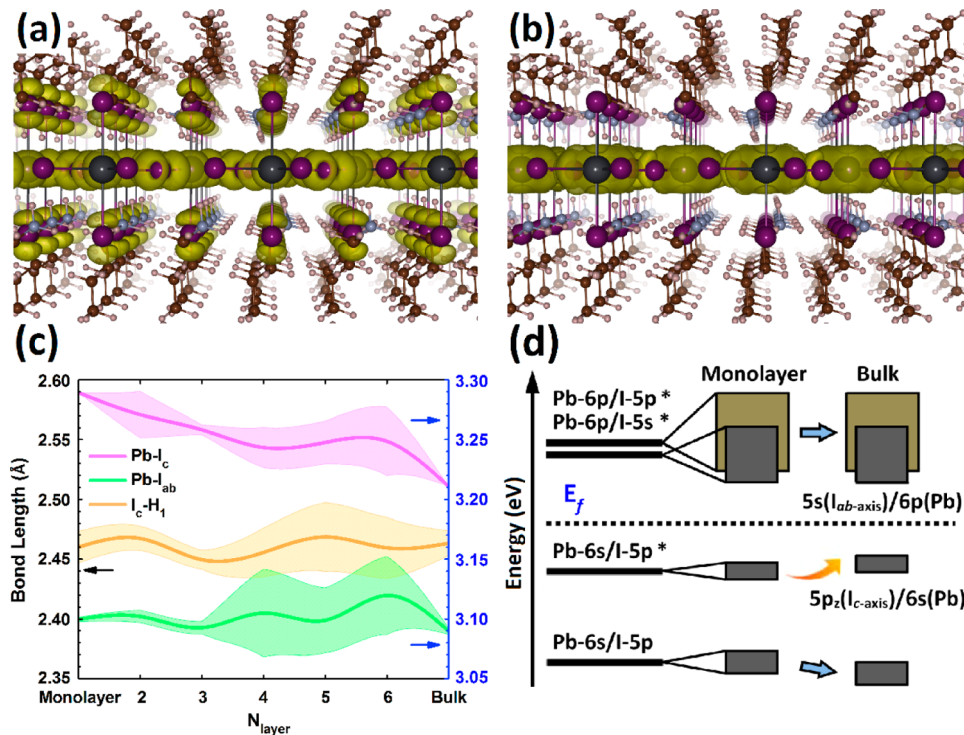


**Figure 4.** Charge densities (yellow isosurfaces) of (a) top of the valence band and (b) bottom of the conduction band at the  $\Gamma$  point calculated with spin-orbit coupling for bulk  $(\text{C}_4\text{H}_9\text{NH}_3)_2\text{PbI}_4$ . (c) The bond length change of Pb-I or I-H bonds, which are given in Figure 1c as a function of layer number. (d) Bonding diagram of monolayer and bulk  $(\text{C}_4\text{H}_9\text{NH}_3)_2\text{PbI}_4$  at the VBM and CBM.

$$E_s = \frac{1}{2} [E_{\text{slab}}^{(\text{C}_4\text{H}_9\text{NH}_3)_2\text{PbI}_4} - \alpha(E_{\text{C}_4\text{H}_9\text{NH}_3} + \mu_{\text{C}_4\text{H}_9\text{NH}_3}) \\ - \beta(E_{\text{Pb}} + \mu_{\text{Pb}}) - \gamma(E_{\text{I}} + \mu_{\text{I}})] \quad (6)$$

where  $E_s$  is the surface energies,  $E_i$  are the energies of the different elements  $i$  in their stable phase,  $E_{(\text{C}_4\text{H}_9\text{NH}_3)_2\text{PbI}_4}$  is the calculated total energies of the slabs. The surface energy relied on the  $\mu_i$  of the component species. In order to evaluate the surface energies, a moderate condition for reactants  $\text{C}_4\text{H}_9\text{NH}_3\text{I}$  and  $\text{PbI}_2$  is chosen in this work, and the chemical potentials of  $\mu_{\text{Pb}}$  and  $\mu_{\text{I}}$  are 1.131 and 0.565 eV, respectively. The corresponding point is labeled as M at the green region in Figure 3a. The calculated surface energies as a function of layer numbers for both  $\text{C}_4\text{H}_9\text{NH}_3\text{I}$  termination ( $\text{C}_4\text{H}_9\text{NH}_3\text{I-T}$ ) and  $\text{PbI}$  termination ( $\text{PbI-T}$ ) slabs in this condition are shown in Figure 3b. The surface energy gradually converges as the number of layers increases. Notably, the  $\text{PbI-T}$  has the relatively larger surface energy than  $\text{C}_4\text{H}_9\text{NH}_3\text{I-T}$ . For the  $\text{PbI-T}$  surface, every atom is connected with other atoms by Pb-I chemical bonds, thus the atomic movement of surface atoms becomes difficult. However, for the  $\text{C}_4\text{H}_9\text{NH}_3\text{I-T}$  surface, the  $\text{C}_4\text{H}_9\text{NH}_3$  ions interact with inorganic cage by weak interactions, thus they could rotate in the cage. The different chemical bonding results in the distinct relaxation of the two surface terminations. The more thermodynamical stable of  $\text{C}_4\text{H}_9\text{NH}_3\text{I-T}$  surfaces indicated that  $\text{C}_4\text{H}_9\text{NH}_3\text{I-T}$  surfaces are favorable during equilibrium growth of  $(\text{C}_4\text{H}_9\text{NH}_3)_2\text{PbI}_4$  perovskites, and the  $\text{PbI-T}$  surface could form only under the  $\text{PbI}_2$ -rich condition. More importantly, as shown in Figure 3b, the surface energy of the  $\text{C}_4\text{H}_9\text{NH}_3\text{I-T}$  surface in 2D  $(\text{C}_4\text{H}_9\text{NH}_3)_2\text{PbI}_4$  perovskite is relatively lower than that of the  $\text{CH}_3\text{NH}_3\text{PbI}_3$  (MAI)-T surface in conventional MAPbX<sub>3</sub> perovskites,<sup>49</sup> confirming the

convenient preparation of atomically thin 2D hybrid perovskites in experiment.

As we confirm the stable surface of  $(\text{C}_4\text{H}_9\text{NH}_3)_2\text{PbI}_4$  perovskites, the absorption properties were further examined. Based on the parabolic approximations, the effective masses ( $m^*/m_e$ ) of carriers, which exist around the VBM and CBM were estimated by fitting the dispersion relation to the following equation:

$$m^*/m_e = \hbar^2 \left[ \frac{\partial^2 \varepsilon(k)}{\partial k^2} \right]^{-1} / m_e \quad (7)$$

where  $k$  is the wave-vector and  $\varepsilon(k)$  is the orbital eigenvalue. From Figure 2b, it is shown that the strong  $s-p$  couplings enhance the dispersions of the upper valence band and result in the small  $m_h^*/m_e$ ; for example, the hole effective mass of bulk  $(\text{C}_4\text{H}_9\text{NH}_3)_2\text{PbI}_4$  is calculated to be 0.269 (as shown in Figure 3c and Table S2), which is smaller than CdTe, CZTSe, CIS, and GaAs, where no  $s-p$  couplings could be found in their valence bands.<sup>11</sup> Also, the calculated  $m_e^*$  and  $m_h^*$  values of bulk  $(\text{C}_4\text{H}_9\text{NH}_3)_2\text{PbI}_4$  were comparable to that in commercial silicon solar energy absorbers.<sup>50,51</sup> The relatively small  $m^*/m_e$  for both holes and electrons and the large absorption efficiencies of the 2D  $(\text{C}_4\text{H}_9\text{NH}_3)_2\text{PbI}_4$  make it an ideal candidate for the solar energy absorber containing the  $p-i-n$  structure.

In practice,  $m^*/m_e$  will change by many elastic scatterings caused by phonon, structural defect, or material size. To check the impact of the thickness on the optical characteristics, the effective masses of photocarriers in  $(\text{C}_4\text{H}_9\text{NH}_3)_2\text{PbI}_4$ , which take thickness effects into account, are estimated. Despite some slight fluctuations from monolayer to bulk  $(\text{C}_4\text{H}_9\text{NH}_3)_2\text{PbI}_4$ , the dispersion at the VBM in a 2D system is lower than that in a 3D system. This results in the larger  $m_h^*/m_e$  found in 2D

$(C_4H_9NH_3)_2PbI_4$ . As a consequence, the mobility of holes in 2D  $(C_4H_9NH_3)_2PbI_4$  decreases conversely. However, the effective masses of the electrons remains almost unchanged with the change of the perovskites thickness. Similarly, the calculated band gaps of  $(C_4H_9NH_3)_2PbI_4$  slabs are sensitive to the thickness of the slab. With the increase of the thickness from single layer to six layers, the band gaps of  $(C_4H_9NH_3)_2PbI_4$  slabs gradually decrease from 2.469 to 2.387 eV, gradually approaching that of the bulk material (2.377 eV).

Another important properties to be unavoidably considered in the mixed halide perovskites are the binding energy between electron and hole, which are generated due to the photon absorption, and the mobility of these charge carriers. The exciton binding energy plays a key role in discriminating whether the charge carriers behave free particles as in normal inorganic 2D semiconductors, or bound excitons as in organic<sup>10</sup> semiconductors. The weaker exciton binding energy indicates more freely behaving charge carriers. After the computations of  $m^*/m_e$ , and the extraction of the static dielectric constants simply from the frequency dependent dielectric constants, we used eq 2 to calculate the exciton binding energy. The calculated data are listed in Figure 4 and Table S2. The calculated exciton binding energy of bulk  $(C_4H_9NH_3)_2PbI_4$  (0.363 eV) based on the hydrogen-like model<sup>37</sup> agrees well with the available experimental values (0.386 eV).<sup>52</sup> Moreover, the exciton binding energies increase with the decreasing layer number ( $N_{layer}$ ) of  $(C_4H_9NH_3)_2PbI_4$ . Based on previous works, the large binding energies can be mainly attributed to the uncommon changing of inorganic/organic structures as well as the effects of dielectric confinements.<sup>53</sup>

In this study, with the decreasing dimensionality of 2D  $(C_4H_9NH_3)_2PbI_4$ , the lower dielectric constant of the organic layer as well as the smaller dispersions near the VBM result in the increase of coulomb interactions between electrons and holes (larger exciton-binding energies). We further calculate the optical absorption coefficients of 2D  $(C_4H_9NH_3)_2PbI_4$  perovskites with the change of layer numbers from eq 5 (see Figure 3d). The absorption peaks redshift from 502 nm for single layer to 519 nm for six layers, and it converges at 522 nm in bulk  $(C_4H_9NH_3)_2PbI_4$ . Although the transition probability is decreased with the reduction of the material size according to the Fermi–Golden rule, its effect is limited; e.g., for monolayer  $(C_4H_9NH_3)_2PbI_4$  perovskites, one remarkable peak could be observed in the visible light region, indicating that the thin 2D  $(C_4H_9NH_3)_2PbI_4$  film can be an effective solar energy absorber in the visible light spectrum.

To understand the change trend of the electronic properties correlated to the material thickness found above, the change in charge densities and bonding characteristics with different dimensionality (2D and 3D) was further examined. Figure 4a,b shows the charge density of VBM and CBM in the bulk  $(C_4H_9NH_3)_2PbI_4$ , respectively. There are two types of I atoms in  $(C_4H_9NH_3)_2PbI_4$  (as shown in Figure 1c): axial I atoms with a chemical bond along the *c* direction ( $I_c$ ) and equatorial I atoms with a chemical bond in the *ab* plane ( $I_{ab}$ ). It can be seen that photogenerated holes at VBM and electrons at CBM located individually; for example, the VBM was contributed by the Pb 6s- $I_c$  5p<sub>z</sub> antibonding orbital, while the CBM is dominated by Pb 6p- $I_{ab}$  5s antibonding orbital (Figure 4a,b,d). As the dimensionality decreased to the monolayer size, the bonding length of Pb- $I_c$  became larger, while the Pb- $I_{ab}$  remained almost unchanged (as shown in Figure 4c and

Table S3). This leads to the weaker hybrid of Pb 6s- $I_c$  5p<sub>z</sub> antibonding orbital at VBM in monolayer  $(C_4H_9NH_3)_2PbI_4$ , while no obvious change of the hybridization between Pb 6p and I<sub>ab</sub> 5s at CBM could be observed, as shown by the bonding diagram in Figure 4d. As a result, the dispersions near the VBM became smaller, and the position of the VBM gradually shifts downward, resulting in an increase of the band gaps as well as the blueshift of the absorption coefficients found in monolayer  $(C_4H_9NH_3)_2PbI_4$ .

In summary, a series of  $(C_4H_9NH_3)_2PbX_4$  (X=Cl, Br and I) perovskites with well-defined 2D layered structures were explored by using DFT calculations. The relatively low surface energy (<10 meV/Å<sup>2</sup>) was found in 2D  $(C_4H_9NH_3)_2PbI_4$ , which confirmed the convenient preparation of atomically thin 2D hybrid perovskites experimentally. Additionally, a clear structures–properties relationship, with the photophysical characteristics directly related to the dimensionality and material compositions, was established. The large *s-p* antibonding couplings in both bulk and monolayer  $(C_4H_9NH_3)_2PbI_4$  lead to small hole/electron effective masses, while  $m_h^*$  increases in proportion to the decreasing inorganic layer thickness. As a result, a slightly shifted band edge emission was found in 2D perovskites; for example, with the increase of perovskite thickness, the absorption peaks redshift from 502 nm for single layer to 519 nm for six layers, and it converged at 522 nm in bulk  $(C_4H_9NH_3)_2PbI_4$ . Although a decreasing transition probability was found with the reduction of the material size in  $(C_4H_9NH_3)_2PbX_4$  perovskite, its effect is limited, indicating that the thin 2D  $(C_4H_9NH_3)_2PbX_4$  film can be an effective solar energy absorber in the visible light spectrum. This study opens up perspectives to fundamentally understand the structure–property relationships in a new family of 2D functional perovskite halides.

## ASSOCIATED CONTENT

### S Supporting Information

The Supporting Information is available free of charge on the ACS Publications website at DOI: [10.1021/acs.jpclett.7b00003](https://doi.org/10.1021/acs.jpclett.7b00003).

Calculated structural and electronic parameters for 2D  $(C_4H_9NH_3)_2PbX_4$  (X=Cl, Br, I) perovskites by different functionals ([PDF](#))

## AUTHOR INFORMATION

### Corresponding Author

\*E-mail address: [limin.liu@csirc.ac.cn](mailto:limin.liu@csirc.ac.cn); Tel: 86-10-82687086.

### ORCID®

Da Wang: [0000-0002-4512-7860](https://orcid.org/0000-0002-4512-7860)

Li-Min Liu: [0000-0003-3925-5310](https://orcid.org/0000-0003-3925-5310)

### Notes

The authors declare no competing financial interest.

## ACKNOWLEDGMENTS

This work was supported by the National Key Research and Development Program of China (Grant No. 2016YFB0700700), the National Natural Science Foundation of China (Grant Nos. 51572016, 11447011, and U1530401), and the China Postdoctoral Science Foundation (Grant No. 2016M590034). The computation supports from Tianhe-2JK computing time award at the Beijing Computational Science Research Center (CSRC) and the Special Program for Applied

Research on Super Computation of the NSFC-Guangdong Joint Fund (the second phase) were also acknowledged.

## ■ REFERENCES

- (1) McGehee, M. D. Perovskite Solar Cells: Continuing to Soar. *Nat. Mater.* **2014**, *13*, 845–846.
- (2) Jeon, N. J.; Noh, J. H.; Yang, W. S.; Kim, Y. C.; Ryu, S.; Seo, J.; Seok, S. I. Compositional Engineering of Perovskite Materials for High-Performance Solar Cells. *Nature* **2015**, *517*, 476–480.
- (3) Yang, W. S.; Noh, J. H.; Jeon, N. J.; Kim, Y. C.; Ryu, S.; Seo, J.; Seok, S. I. High-Performance Photovoltaic Perovskite Layers Fabricated through Intramolecular Exchange. *Science* **2015**, *348*, 1234.
- (4) Zhou, H.; Chen, Q.; Li, G.; Luo, S.; Song, T.-b.; Duan, H.-S.; Hong, Z.; You, J.; Liu, Y.; Yang, Y. Interface Engineering of Highly Efficient Perovskite Solar Cells. *Science* **2014**, *345*, 542.
- (5) Lee, M. M.; Teuscher, J.; Miyasaka, T.; Murakami, T. N.; Snaith, H. J. Efficient Hybrid Solar Cells Based on Meso-Superstructured Organometal Halide Perovskites. *Science* **2012**, *338*, 643.
- (6) Green, M. A.; Jiang, Y.; Soufiani, A. M.; Ho-Baillie, A. Optical Properties of Photovoltaic Organic-Inorganic Lead Halide Perovskites. *J. Phys. Chem. Lett.* **2015**, *6*, 4774–4785.
- (7) Pellet, N.; Gao, P.; Gregori, G.; Yang, T.-Y.; Nazeeruddin, M. K.; Maier, J.; Grätzel, M. Mixed-Organic-Cation Perovskite Photovoltaics for Enhanced Solar-Light Harvesting. *Angew. Chem., Int. Ed.* **2014**, *53*, 3151–3157.
- (8) Chen, Q.; Zhou, H.; Hong, Z.; Luo, S.; Duan, H.-S.; Wang, H.-H.; Liu, Y.; Li, G.; Yang, Y. Planar Heterojunction Perovskite Solar Cells Via Vapor-Assisted Solution Process. *J. Am. Chem. Soc.* **2014**, *136*, 622–625.
- (9) Eperon, G. E.; Stranks, S. D.; Menelaou, C.; Johnston, M. B.; Herz, L. M.; Snaith, H. J. Formamidinium Lead Trihalide: A Broadly Tunable Perovskite for Efficient Planar Heterojunction Solar Cells. *Energy Environ. Sci.* **2014**, *7*, 982–988.
- (10) Malinkiewicz, O.; Yella, A.; Lee, Y. H.; Espallargas, G. M.; Graetzel, M.; Nazeeruddin, M. K.; Bolink, H. J. Perovskite Solar Cells Employing Organic Charge-Transport Layers. *Nat. Photonics* **2014**, *8*, 128–132.
- (11) Yin, W.-J.; Shi, T.; Yan, Y. Unique Properties of Halide Perovskites as Possible Origins of the Superior Solar Cell Performance. *Adv. Mater.* **2014**, *26*, 4653–4658.
- (12) Yin, W.-J.; Shi, T.; Yan, Y. Unusual Defect Physics in  $\text{CH}_3\text{NH}_3\text{PbI}_3$  Perovskite Solar Cell Absorber. *Appl. Phys. Lett.* **2014**, *104*, 063903.
- (13) Mosconi, E.; Umari, P.; De Angelis, F. Electronic and Optical Properties of Mixed Sn-Pb Organohalide Perovskites: A First Principles Investigation. *J. Mater. Chem. A* **2015**, *3*, 9208–9215.
- (14) Zhang, L.; Sit, P. H. L. Ab Initio Study of Interaction of Water, Hydroxyl Radicals, and Hydroxide Ions with  $\text{CH}_3\text{NH}_3\text{PbI}_3$  and  $\text{CH}_3\text{NH}_3\text{PbBr}_3$  Surfaces. *J. Phys. Chem. C* **2015**, *119*, 22370–22378.
- (15) Even, J.; Pedesseau, L.; Katan, C.; Kepeñekian, M.; Lauret, J.-S.; Sapori, D.; Deleporte, E. Solid-State Physics Perspective on Hybrid Perovskite Semiconductors. *J. Phys. Chem. C* **2015**, *119*, 10161–10177.
- (16) Mitzi, D. B. Synthesis, Structure, and Properties of Organic-Inorganic Perovskites and Related Materials. *Prog. Inorg. Chem.* **1999**, *48*, 1–121.
- (17) Boix, P. P.; Agarwala, S.; Koh, T. M.; Mathews, N.; Mhaisalkar, S. G. Perovskite Solar Cells: Beyond Methylammonium Lead Iodide. *J. Phys. Chem. Lett.* **2015**, *6*, 898–907.
- (18) Smith, I. C.; Hoke, E. T.; Solis-Ibarra, D.; McGehee, M. D.; Karunadasa, H. I. A Layered Hybrid Perovskite Solar-Cell Absorber with Enhanced Moisture Stability. *Angew. Chem.* **2014**, *126*, 11414–11417.
- (19) Cao, D. H.; Stoumpos, C. C.; Farha, O. K.; Hupp, J. T.; Kanatzidis, M. G. 2d Homologous Perovskites as Light-Absorbing Materials for Solar Cell Applications. *J. Am. Chem. Soc.* **2015**, *137*, 7843–7850.
- (20) Koh, T. M.; Shanmugam, V.; Schlipf, J.; Oesinghaus, L.; Müller-Buschbaum, P.; Ramakrishnan, N.; Swamy, V.; Mathews, N.; Boix, P.; Mhaisalkar, S. G. Nanostructuring Mixed-Dimensional Perovskites: A Route toward Tunable, Efficient Photovoltaics. *Adv. Mater.* **2016**, *28*, 3653–3661.
- (21) Sichert, J. A.; Tong, Y.; Mutz, N.; Vollmer, M.; Fischer, S.; Milowska, K. Z.; Cortadella, R. G.; Nickel, B.; Daw, C. C.; Stolarczyk, J. K.; et al. Quantum Size Effect in Organometal Halide Perovskite Nanoplatelets. *Nano Lett.* **2015**, *15*, 6521–6527.
- (22) Dou, L.; Wong, A. B.; Yu, Y.; Lai, M. L.; Kornienko, N.; Eaton, S. W.; Fu, A.; Bisshak, C. G.; Ma, J.; Ding, T.; et al. Atomically Thin Two-Dimensional Organic-Inorganic Hybrid Perovskites. *Science* **2015**, *349*, 1518.
- (23) Quan, L. N.; Yuan, M.; Comin, R.; Voznyy, O.; Beauregard, E. M.; Hoogland, S.; Buin, A.; Kirmani, A. R.; Zhao, K.; Amassian, A.; et al. Ligand-Stabilized Reduced-Dimensionality Perovskites. *J. Am. Chem. Soc.* **2016**, *138*, 2649–2655.
- (24) Niu, W.; Eiden, A.; Vijaya Prakash, G.; Baumberg, J. J. Exfoliation of Self-Assembled 2d Organic-Inorganic Perovskite Semiconductors. *Appl. Phys. Lett.* **2014**, *104*, 171111.
- (25) Geim, A. K.; Grigorieva, I. V. Van Der Waals Heterostructures. *Nature* **2013**, *499*, 419–425.
- (26) González-Carrero, S.; Galian, R. E.; Pérez-Prieto, J. Organometal Halide Perovskites: Bulk Low-Dimension Materials and Nanoparticles. *Part. Part. Syst. Char.* **2015**, *32*, 709–720.
- (27) Liu, J.; Xue, Y.; Wang, Z.; Xu, Z. Q.; Zheng, C.; Weber, B.; Song, J.; Wang, Y.; Lu, Y.; Zhang, Y.; et al. Two-Dimensional  $\text{CH}_3\text{NH}_3\text{PbI}_3$  Perovskite: Synthesis and Optoelectronic Application. *ACS Nano* **2016**, *10*, 3536–3542.
- (28) Kresse, G.; Furthmüller, J. Efficient Iterative Schemes for Ab Initio Total-Energy Calculations Using a Plane-Wave Basis Set. *Phys. Rev. B: Condens. Matter Mater. Phys.* **1996**, *54*, 11169–11186.
- (29) Kresse, G.; Furthmüller, J. Efficiency of Ab-Initio Total Energy Calculations for Metals and Semiconductors Using a Plane-Wave Basis Set. *Comput. Mater. Sci.* **1996**, *6*, 15–50.
- (30) Blöchl, P. E. Projector Augmented-Wave Method. *Phys. Rev. B: Condens. Matter Mater. Phys.* **1994**, *50*, 17953–17979.
- (31) Kresse, G.; Joubert, D. From Ultrasoft Pseudopotentials to the Projector Augmented-Wave Method. *Phys. Rev. B: Condens. Matter Mater. Phys.* **1999**, *59*, 1758–1775.
- (32) Blöchl, P. E.; Först, C. J.; Schimpl, J. Projector Augmented Wave Method:Ab Initio Molecular Dynamics with Full Wave Functions. *Bull. Mater. Sci.* **2003**, *26*, 33–41.
- (33) Grimme, S.; Antony, J.; Ehrlich, S.; Krieg, H. A Consistent and Accurate Ab Initio Parametrization of Density Functional Dispersion Correction (DFT-D) for the 94 Elements H–Pu. *J. Chem. Phys.* **2010**, *132*, 154104.
- (34) Perdew, J. P.; Chevary, J. A.; Vosko, S. H.; Jackson, K. A.; Pederson, M. R.; Singh, D. J.; Fiolhais, C. Atoms, Molecules, Solids, and Surfaces: Applications of the Generalized Gradient Approximation for Exchange and Correlation. *Phys. Rev. B: Condens. Matter Mater. Phys.* **1992**, *46*, 6671–6687.
- (35) Heyd, J.; Scuseria, G. E.; Ernzerhof, M. Hybrid Functionals Based on a Screened Coulomb Potential. *J. Chem. Phys.* **2006**, *124*, 219906.
- (36) Read, A. J.; Needs, R. J. Calculation of Optical Matrix Elements with Nonlocal Pseudopotentials. *Phys. Rev. B: Condens. Matter Mater. Phys.* **1991**, *44*, 13071–13073.
- (37) Jong, U.-G.; Yu, C.-J.; Ri, J.-S.; Kim, N.-H.; Ri, G.-C. Influence of Halide Composition on the Structural, Electronic, and Optical Properties of Mixed  $\text{CH}_3\text{NH}_3\text{Pb}(\text{I}_{1-x}\text{Br}_x)_3$  Perovskites Calculated Using the Virtual Crystal Approximation Method. *Phys. Rev. B: Condens. Matter Mater. Phys.* **2016**, *94*, 125139.
- (38) Xiao, Z.; Hiramatsu, H.; Ueda, S.; Toda, Y.; Ran, F.-Y.; Guo, J.; Lei, H.; Matsuishi, S.; Hosono, H.; Kamiya, T. Narrow Bandgap in  $\text{B}-\text{BaZn}_2\text{As}_2$  and Its Chemical Origins. *J. Am. Chem. Soc.* **2014**, *136*, 14959–14965.
- (39) Even, J.; Pedesseau, L.; Jancu, J.-M.; Katan, C. Importance of Spin-Orbit Coupling in Hybrid Organic/Inorganic Perovskites for Photovoltaic Applications. *J. Phys. Chem. Lett.* **2013**, *4*, 2999–3005.
- (40) Mitzi, D. B.; Chondroudis, K.; Kagan, C. R. Organic-Inorganic Electronics. *IBM J. Res. Dev.* **2001**, *45*, 29–45.

- (41) Du, M. H. Efficient Carrier Transport in Halide Perovskites: Theoretical Perspectives. *J. Mater. Chem. A* **2014**, *2*, 9091–9098.
- (42) Du, M.-H. Density Functional Calculations of Native Defects in  $\text{CH}_3\text{NH}_3\text{PbI}_3$ : Effects of Spin-Orbit Coupling and Self-Interaction Error. *J. Phys. Chem. Lett.* **2015**, *6*, 1461–1466.
- (43) Walsh, A.; Payne, D. J.; Egdell, R. G.; Watson, G. W. Stereochemistry of Post-Transition Metal Oxides: Revision of the Classical Lone Pair Model. *Chem. Soc. Rev.* **2011**, *40*, 4455–4463.
- (44) Saparov, B.; Mitzi, D. B. Organic-Inorganic Perovskites: Structural Versatility for Functional Materials Design. *Chem. Rev.* **2016**, *116*, 4558–4596.
- (45) Shockley, W.; Queisser, H. J. Detailed Balance Limit of Efficiency of P-N Junction Solar Cells. *J. Appl. Phys.* **1961**, *32*, 510–519.
- (46) Liu, M.; Johnston, M. B.; Snaith, H. J. Efficient Planar Heterojunction Perovskite Solar Cells by Vapour Deposition. *Nature* **2013**, *501*, 395–398.
- (47) Shah, A.; Torres, P.; Tscharner, R.; Wyrsch, N.; Keppner, H. Photovoltaic Technology: The Case for Thin-Film Solar Cells. *Science* **1999**, *285*, 692.
- (48) Gratzel, M. The Light and Shade of Perovskite Solar Cells. *Nat. Mater.* **2014**, *13*, 838–842.
- (49) Geng, W.; Tong, C.-J.; Liu, J.; Zhu, W.; Lau, W.-M.; Liu, L.-M. Structures and Electronic Properties of Different  $\text{CH}_3\text{NH}_3\text{PbI}_3/\text{TiO}_2$  Interface: A First-Principles Study. *Sci. Rep.* **2016**, *6*, 20131.
- (50) Gray, D. E. *American Institute of Physics Handbook*; McGraw-Hill: New York, 1982.
- (51) Lide, D. R. *CRC Handbook of Chemistry and Physics*; CRC Press: Boca Raton, FL, 2004.
- (52) Hirasawa, M.; Ishihara, T.; Goto, T.; Uchida, K.; Miura, N. Magnetoabsorption of the Lowest Exciton in Perovskite-Type Compound  $(\text{CH}_3\text{NH}_3)\text{PbI}_3$ . *Phys. B* **1994**, *201*, 427–430.
- (53) Cheng, Z.; Lin, J. Layered Organic-Inorganic Hybrid Perovskites: Structure, Optical Properties, Film Preparation, Patterning and Templating Engineering. *CrystEngComm* **2010**, *12*, 2646–2662.